NANOMATERIALS

Interface and heterostructure design in polyelemental nanoparticles

Peng-Cheng Chen[1,2], Mohan Liu[1], Jingshan S. Du[1,2], Brian Meckes[2,3], Shunzhi Wang[2,3], Haixin Lin[2,3], Vinayak P. Dravid[1,2], Chris Wolverton[1], Chad A. Mirkin[1,2,3]*

Nanomaterials that form as heterostructures have applications in catalysis, plasmonics, and electronics. Multielement nanoparticles can now be synthesized through a variety of routes, but how thermodynamic phases form in such structures and how specific interfaces between them can be designed and synthesized are still poorly understood. We explored how palladium-tin alloys form mixed-composition phases with metals with known but complex miscibilities. Nanoparticles with up to seven elements were synthesized, and many form triphase heterostructures consisting of either three-interface or two-interface architectures. Density functional theory calculations and experimental work were used to determine the balance between the surface and interfacial energies of the observed phases. From these observations, design rules have been established for making polyelemental systems with specific heterostructures, including tetraphase nanoparticles with as many as six junctions.

The interfaces created by phase boundaries in multiphase nanoparticles (NPs) not only architecturally define the NPs (*1*–*4*) but also introduce internal structural discontinuity (*5*) and facilitate electronic interactions between adjacent domains (*6*, *7*). For example, charge transfer occurring across an NP interface can be used to tune plasmonic and catalytic properties (*8*–*12*). In addition, strain engineering can modulate the electronic structures of materials when the nearby phases are epitaxial (*13*), and the interface between two domains may be rich in high-energy defects that can enhance catalysis (*3*, *14*, *15*). Lastly, a single NP with multiple interfaces can exhibit collective properties that are not observed in particles comprising the individual components (in terms of both the composition and the number and types of interfaces) (*16*, *17*). As the field of multiphase, polyelemental NPs progresses toward greater compositional diversity and structural complexity (*1*, *2*, *18*–*21*), understanding how specific classes of interfaces can be established in one particle is crucial for designing new and functional nanostructures. Although NPs have been synthesized and characterized with up to four phases (*1*, *2*, *21*–*30*), there is limited general understanding of why specific architectures form, and the role of surface and interfacial energies in controlling the architecture of NPs with more than two phases is not fully understood.

In this study, we used scanning probe block copolymer lithography (SPBCL), which uses lithographically defined polymer domes as nanoreactors to synthesize multimetallic NPs to study polyelemental systems (*19*). We used substrates amenable to both electron microscopy characterization and thermal annealing so that the NPs reached thermodynamic equilibrium. These studies, in combination with density functional theory (DFT) calculations, allowed us to identify miscibility gaps between PdSn alloys and other metals (Au, Ag, Cu, Co, and Ni) and construct a library of compositionally and structurally related multiphase NPs. On the basis of the resulting NP architectures, we establish design rules for synthesizing thermally stable polyelemental heterostructures with increasing complexity, culminating in an unprecedented tetraphase NP made from Au, Co, Pd, Sn, and Ni with six phase boundaries. Core-shell structures were not considered because they were not experimentally observed. We focus on the number and types of interfaces that can be formed in one heterostructured NP, rather than placing any constraints on the morphology of the NPs and interfaces.

Number of possible interfaces in multiphase NPs

Observation 1: For a polyelemental NP with n phases, the number of possible interfaces is between $n - 1$ and $n(n - 1)/2$.

For an n-phase NP, the maximum number of different interfaces is $n(n - 1)/2$ if all phases can be interconnected, and the minimum number of different interfaces is $(n - 1)$, which occurs when the n phases form a layered structure, with each stripe defining a different phase. Therefore, triphase NPs are either heterotrimers with two interfaces or pie-shaped particles with three interfaces. Tetraphase NPs can have three to six interfaces (fig. S1). To experimentally determine whether these combinations of interfaces exist, we report a systematic study of a septenary system consisting of particles containing combinations of Au, Ag, Cu, Co, Ni, Pd, and Sn, resulting in a set of NPs with as many as four phases. According to bulk phase diagrams, Pd and Sn are miscible with the other five elements, forming either solid solutions or intermetallics (*31*). However, when we combined three elements consisting of AuPdSn or CoPdSn into one NP and subjected the NP to annealing under H_2 at 500°C for 24 hours, heterodimers with PdSn domains and Au or Co domains were obtained (figs. S2 and S3). Annular dark-field scanning transmission electron microscopy (ADF-STEM) images of Au-PdSn and Co-PdSn NPs (where the hyphen separates different phases) (table S1) show dimeric structures, with the contrast mainly from the difference in atomic number between PdSn and Au or between PdSn and Co. Energy-dispersive x-ray spectroscopy (EDS) analysis further verified the separation of the elements in Au-PdSn and Co-PdSn heterodimers (fig. S3).

To understand why this phase separation was observed, we used DFT calculations of the formation energies (ΔH_f) of all known compounds (including unary, binary, and ternary) in the AuPdSn and CoPdSn systems, which are from the Open Quantum Materials Database (table S2) (*32*, *33*). With the ΔH_f of all compounds, we computed the energetics of all phases as well as all linear combinations of phases for a given composition, evaluated by using the grand canonical linear programming (GCLP) method (*34*). The GCLP calculation allowed us to determine the thermodynamic ground-state phase or collection of phases at 0 K, which gives us a good prediction for the stable phases of a polyelemental system with a given composition. For an equal mixture of either Au or Co with Pd and Sn, we identified the stable phases as PdSn and either Au or Co (i.e., X-PdSn, where X is Au or Co). To verify the simulation, we examined the thermal stability of the Au-PdSn and Co-PdSn heterodimers by heating the NPs to temperatures between 500° and 750°C (fig. S4 and S5), with the upper end of the range near the melting temperature of bulk Au (1064°C) and far beyond that of bulk Sn (232°C). Experimentally, for both Au-PdSn and Co-PdSn, heterodimers were stable after being temperature ramped between 500° and 750°C for 48 hours, supporting the conclusion that the observed phase separation was not a kinetic result. Given the low miscibility between Au and Co (fig. S3A) (*19*), PdSn, Au, and Co constitute a useful set of building blocks for constructing higher-order heterostructured NPs.

Triphase NPs with two or three interfaces

Observation 2: Biphase structures cannot be used to predict the architecture of structures with three or more phases.

We previously reported that the Ag-Cu-Co triphase system adopts a two-interface architecture, with a central Cu domain capped by Ag and Co domains (fig. S6) (*19*). However, EDS mapping revealed that the four-element Au-Co-PdSn NPs synthesized by SPBCL separated into three interconnected domains, a Au (yellow), a Co (green), and a PdSn domain (blue-purple, consisting of a compositional variation, e.g., Pd_3Sn, Pd_2Sn,

[1]Department of Materials Science and Engineering, Northwestern University, Evanston, IL 60208, USA. [2]International Institute for Nanotechnology, Northwestern University, Evanston, IL 60208, USA. [3]Department of Chemistry, Northwestern University, Evanston, IL 60208, USA.
*Corresponding author. Email: chadnano@northwestern.edu

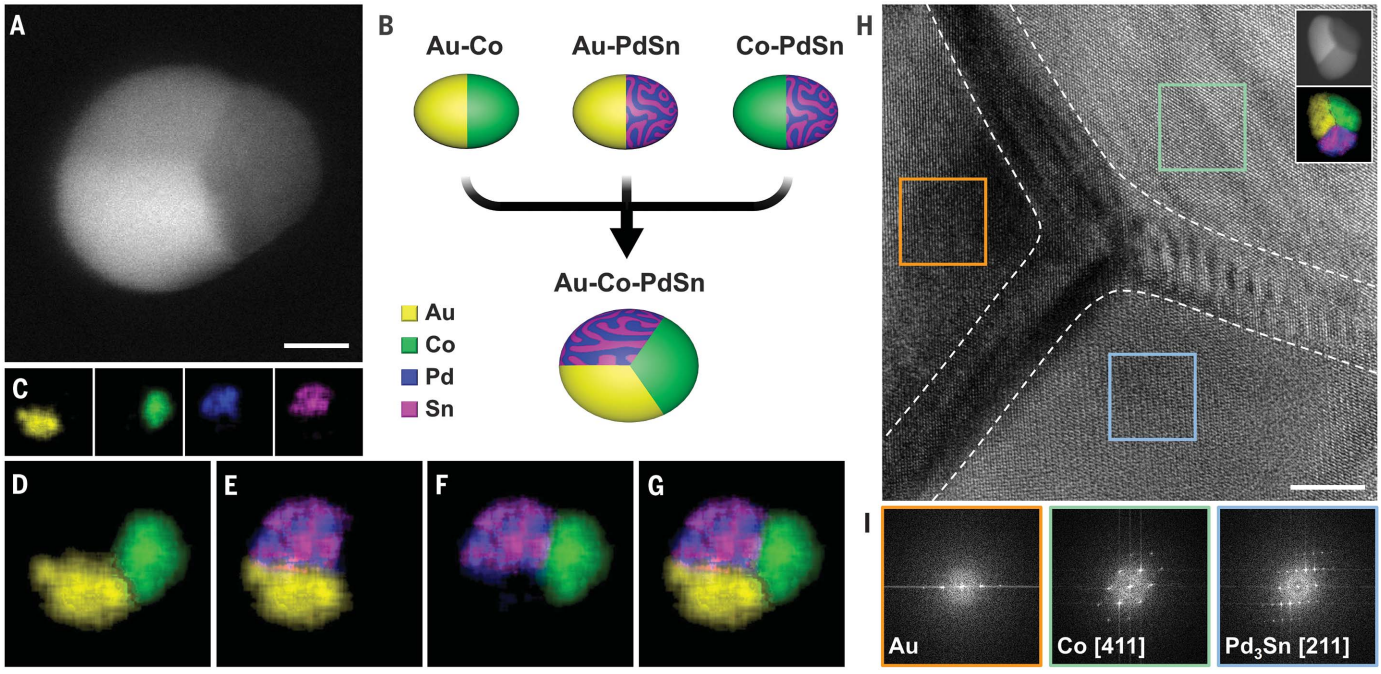

Fig. 1. Au-Co-PdSn triphase heterostructured NPs with three interconnected interfaces. (**A**) ADF-STEM image of a representative Au-Co-PdSn NP ($Au_{0.30}Co_{0.37}Pd_{0.19}Sn_{0.14}$). Scale bar, 10 nm. (**B**) Schematic illustration of the miscibility relationship among the Au, Co, and PdSn phases. (**C** to **F**) EDS elemental mapping of the NP in (A). Overlay of selected element maps shows the phase boundaries of (D) Au-Co, (E) Au-PdSn, and (F) Co-PdSn. (**G**) Overlay of all element maps showing the configuration of the three phases in a Au-Co-PdSn NP. (**H**) HRTEM image of the triphase junction in a Au-Co-PdSn NP ($Au_{0.25}Co_{0.36}Pd_{0.29}Sn_{0.10}$). Scale bar, 3 nm. Dashed lines highlight the positions of the three phase boundaries. Insets are an ADF-STEM image and EDS mapping of the entire NP. (**I**) FFTs of the regions indicated in the HRTEM image.

or PdSn) (Fig. 1, A to G, and figs. S7 to S10). The blotchy EDS map of the PdSn domain indicates a nonuniform distribution of Pd and Sn at the atomic scale, which is caused primarily by the coexistence of multiple PdSn intermetallic phases in the PdSn domain (see the supplementary materials for detailed discussion). The STEM image contrast among the three domains is attributed to differences in atomic number (Fig. 1A). The orientation of the phase boundaries in the triphase NPs is random with respect to the substrate [a SiN_x transmission electron microscopy (TEM) grid with a native oxide top layer (where x is a variable representing the number of nitrogen atoms)] (fig. S11), indicating that none of the metal phases exhibit preferential binding to the substrate. In addition to SiN_x grids, we used Cu TEM grids with carbon support films and observed similar Au-Co-PdSn triphase structures (pie-shaped architectures in fig. S12). Taken together, these data suggest that the SiN_x substrates have little effect in dictating the phase separation and interface development of the NPs we have studied. Substrate effects may be more pronounced and need to be taken into account when the interactions between NPs and substrates are strong (e.g., for oxide NPs formed on oxide supports). For simplicity, particles with phase boundaries perpendicular to the substrate are used to clearly show the positions of different phases.

High-resolution transmission electron microscopy (HRTEM) characterization of a triphase junction in a Au-Co-Pd_3Sn NP confirmed the formation of solid-state interfaces among three domains (Fig. 1H and fig. S13). Fast Fourier transformations (FFTs) of different regions indicate that Co is oriented along the [411] zone axis of a face-centered cubic crystal structure and Pd_3Sn is oriented along the [211] zone axis (Fig. 1I). The FFT of the Au domain shows only reflections that can be assigned to Au {311} planes. Experimentally, no specific relationship among the lattice structures of the three domains was observed (figs. S14 to S18). Although the crystal structure of the interfaces within Au-Co-PdSn NPs differs from one particle to another, all of the domains in the NPs are in a three-interface configuration (figs. S17 and S18). Similar to the Au-Co-PdSn system, Ag and Co also formed biphase heterodimers (*19*), so in principle, this interface could have been present in the Ag-Cu-Co triphase NP, but it was not actually observed (fig. S6). Thus, the presence of interfaces in biphase architectures alone cannot be used to predict whether those interfaces will form in triphase NPs.

Observation 3: Thermodynamic architectures are a consequence of the balance between surface and interfacial energies (e.g., for a three-phase structure, dictating the likelihood of a three-interface or two-interface architecture).

To understand why different architectures form in triphase NPs, we performed DFT calculations to determine the total surface and interfacial energies of Au-Co-Pd_3Sn and Ag-Cu-Co triphase NPs for all possible architectures. For the Au-Co-Pd_3Sn triphase system, interface models were set up with each material domain composed of (111) atom planes (Fig. 2A, figs. S19 to S21, and tables S3 to S5). To minimize the interfacial energy, all interfacial supercells were fully relaxed with respect to volume as well as all cell-internal and cell-external degrees of freedom. The three calculated interfacial energies along with three calculated surface energies were combined to evaluate the total energy of NPs by using spherical models that have equal volumes of each phase (Fig. 2B, fig. S20, and table S4). As shown in Fig. 2C, Au-Co-Pd_3Sn NPs with three-interface architectures had the lowest total energy. By contrast, DFT energetics of the Ag-Cu-Co triphase system revealed that two-interface architectures with Cu as the central domain had the lowest total energy (Fig. 2, D to F). Thus, the preferential architecture of each triphase NP is the one that minimizes the combined surface and interfacial energies.

Although the DFT calculations were performed on models with idealized interfacial structures and NP morphologies that do not perfectly match the actual NPs (figs. S17 and S18), the architectures of triphase NPs synthesized by SPBCL match the predictions of the lowest-energy morphologies. We hypothesized that the annealing provides sufficient time and energy for the NPs to reconfigure their architectures to the thermodynamic state. When we kinetically froze the annealing process for the Au-Co-PdSn triphase NPs after 0.5 and 1.5 hours at 500°C (figs. S22 to S24), complex kinetics were observed, with intraparticle

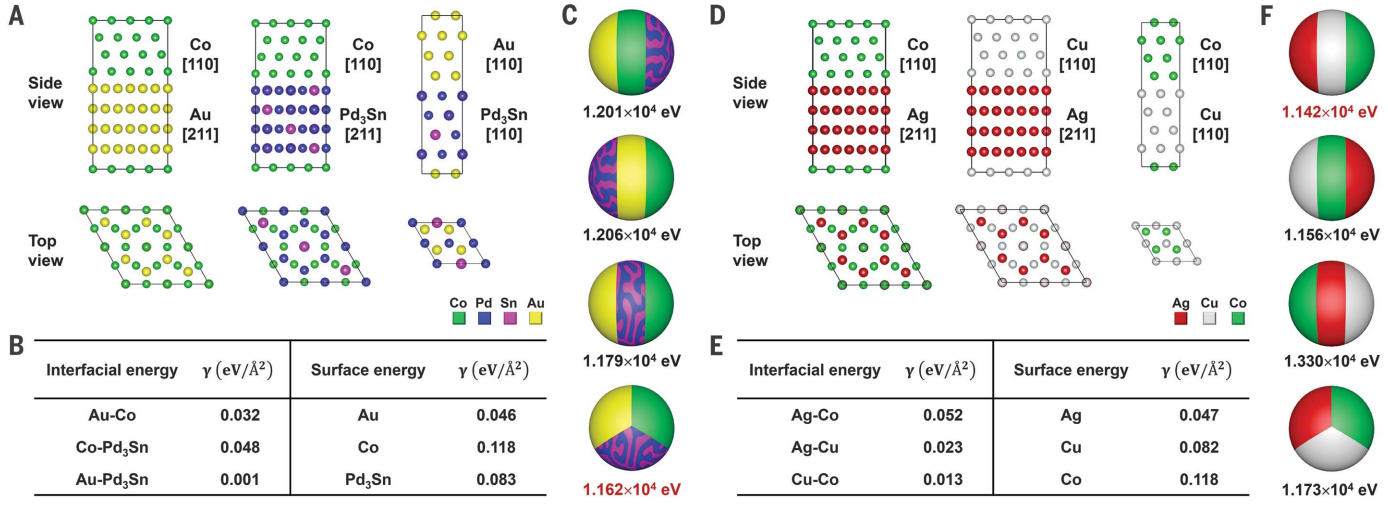

B

Interfacial energy	γ (eV/Å²)	Surface energy	γ (eV/Å²)
Au-Co	0.032	Au	0.046
Co-Pd_3Sn	0.048	Co	0.118
Au-Pd_3Sn	0.001	Pd_3Sn	0.083

E

Interfacial energy	γ (eV/Å²)	Surface energy	γ (eV/Å²)
Ag-Co	0.052	Ag	0.047
Ag-Cu	0.023	Cu	0.082
Cu-Co	0.013	Co	0.118

Fig. 2. DFT simulation of the architecture of Au-Co-Pd_3Sn and Ag-Cu-Co triphase NPs. (**A**) DFT-simulated relaxed structures of the (111) interfacial planes among Au, Co, and Pd_3Sn. (**B**) The surface energies of Au, Co, and Pd_3Sn (111) planes and the interfacial energies among Au, Co, and Pd_3Sn (111) planes. γ, surface and interfacial energies. (**C**) Calculated total surface and interfacial energies of Au-Co-Pd_3Sn NPs with equal volumes of each phase (diameter, 20 nm). (**D**) DFT-simulated relaxed structures of the (111) interfacial planes among Ag, Cu, and Co. (**E**) The surface energies of Ag, Cu, and Co (111) planes and the interfacial energies among Ag, Cu, and Co (111) planes. (**F**) Calculated total surface and interfacial energies of Ag-Cu-Co NPs with equal volumes of each phase (diameter, 20 nm).

coarsening leading to particles with three distinct metal domains (fig. S22). Because of the randomness of the metal element aggregation within the polymer nanoreactors (*35*), the element distribution was different within such architectures. Specifically, for the Au-Co-PdSn NP system, triphase NPs containing only two interfaces were observed as kinetic products (where any of the three domains consisting of Au, Co, or PdSn formed the central domain) (Fig. 3). Continued annealing at 500°C transformed the Au-Co-PdSn NPs into three-interface architectures (Fig. 3A), likely through the motion of surface atoms on the NP. Experimentally, the majority of Au-Co-PdSn NPs were converted into a three-interface architecture (architectural yield, ~75%; sample size, 150) (Fig. 3B). The remaining NPs remained kinetically trapped, and longer annealing times or higher annealing temperatures would be required to transform them into the thermodynamic three-interface architectures. When the NPs were annealed for longer times (5 days) and at a higher temperature (750°C), the two-interface NPs evolved into three-interface structures whereas the three-interface NPs remained relatively unchanged (figs. S25 and S26). The evaporative loss of Sn under such conditions prevents achieving 100% yields of the three-interface NPs with fixed compositions. We validated the Au-Co-PdSn (three-interface) and Ag-Cu-Co (two-interface) thermodynamic NP structures for particle sizes between 15 and 60 nm. If the NP size was reduced, the strain in the NP, which contributes to the total surface and interfacial energies, would change, and therefore, the thermodynamically preferred architectures may also change. Experimentally, it is challenging to characterize heterostructured NPs with small domains by EDS mapping.

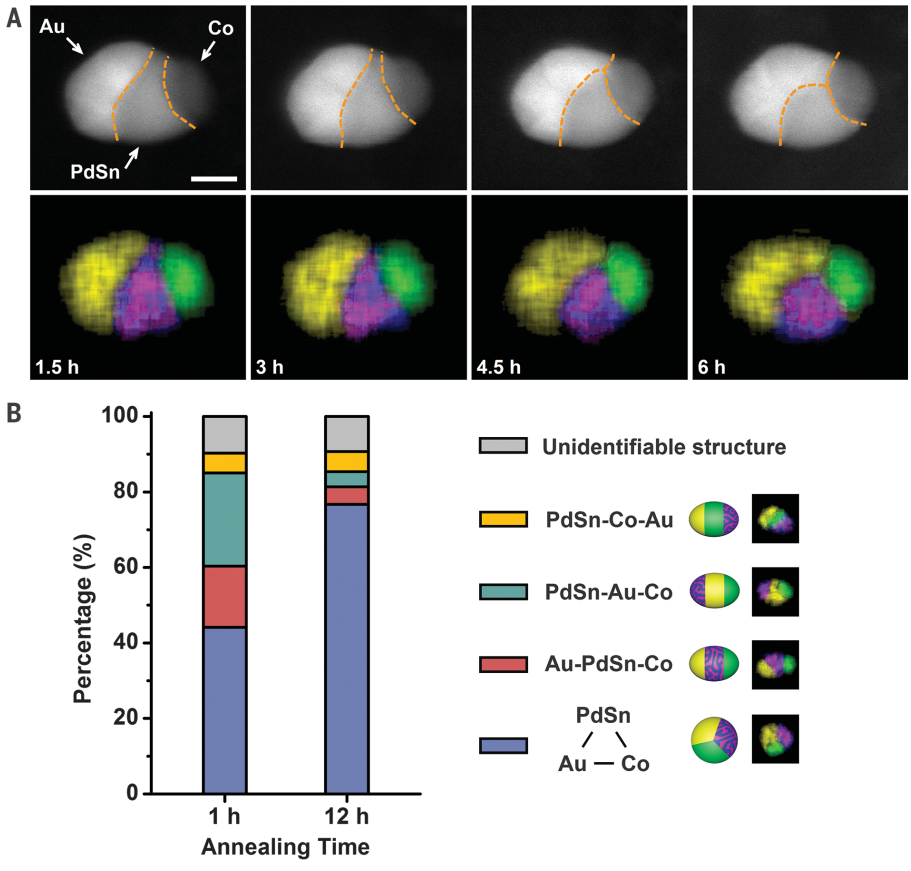

Fig. 3. Structural evolution of Au-Co-PdSn triphase NPs during thermal annealing. (**A**) ADF-STEM images (top row) and corresponding EDS mapping (bottom row) of a Au-Co-PdSn NP ($Au_{0.33}Co_{0.24}Pd_{0.26}Sn_{0.17}$) annealed under flowing H_2 at 500°C over time. Dashed lines outline the positions of phase boundaries. Scale bar, 15 nm. (**B**) Statistical distributions of NPs (n = 150) with different architectures.

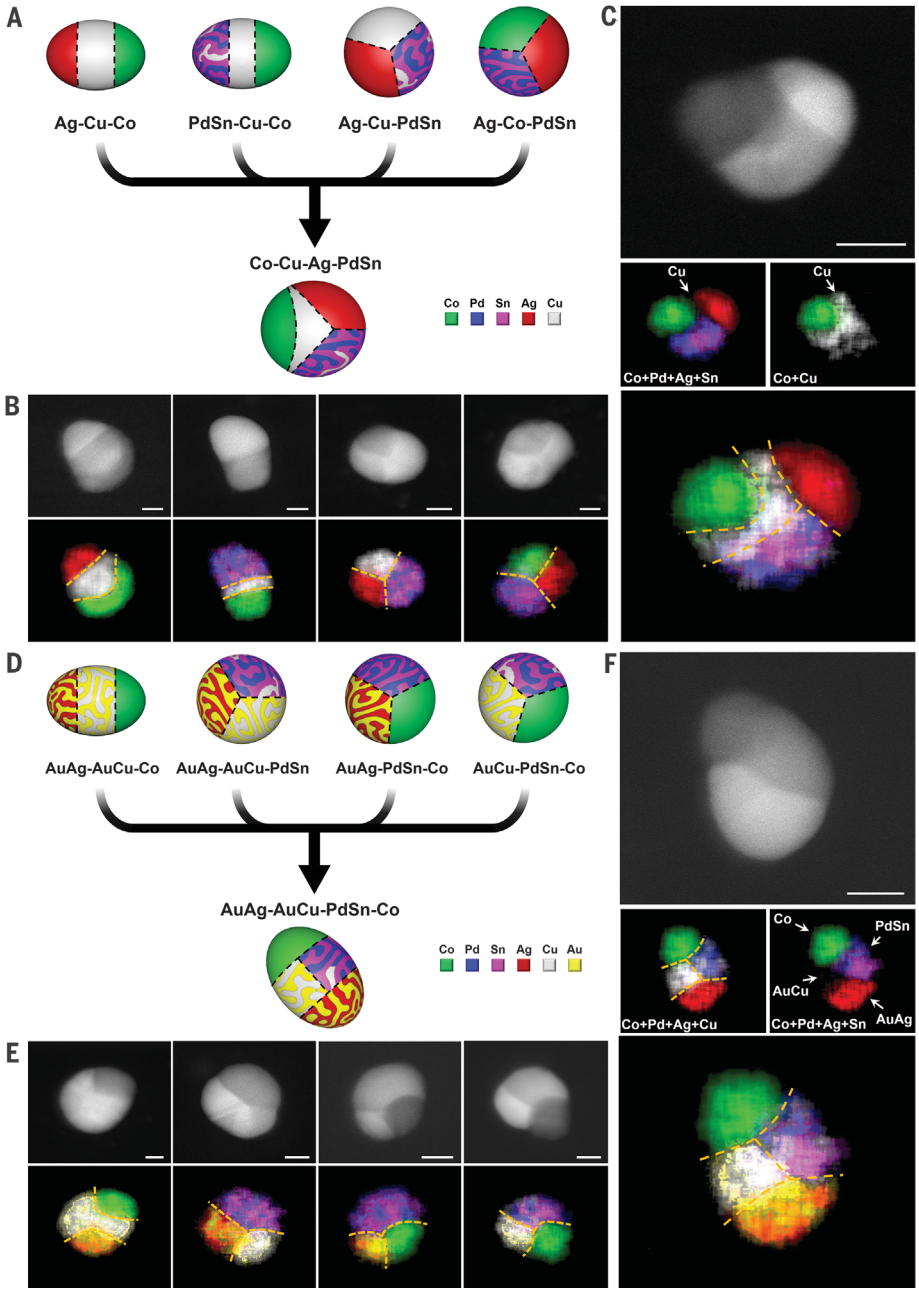

Fig. 4. Tetraphase heterostructured NPs with four and five interfaces. (**A**) Schematic illustration depicting the architectures of tri- and tetraphase NPs composed of Ag, Cu, Co, and PdSn phases. Dashed lines outline the positions of the phase boundaries. (**B**) ADF-STEM images (top row) and EDS mapping (bottom row) of representative triphase NPs for all phase combinations. The compositions of the four triphase NPs are $Ag_{0.23}Cu_{0.47}Co_{0.30}$, $Co_{0.34}Cu_{0.29}Pd_{0.21}Sn_{0.16}$, $Ag_{0.30}Cu_{0.30}Pd_{0.27}Sn_{0.13}$, and $Ag_{0.33}Co_{0.23}Pd_{0.27}Sn_{0.17}$. (**C**) ADF-STEM image (top row) and EDS mapping (bottom row) of a representative tetraphase NP composed of Ag, Cu, Co, and PdSn phases ($Ag_{0.32}Cu_{0.20}Co_{0.21}Pd_{0.15}Sn_{0.12}$). Overlay of selected element maps (middle row) reveals the relative positions of the four phases in the NP. (**D**) Schematic illustration depicting the architectures of tri- and tetraphase NPs composed of AuAg, AuCu, Co, and PdSn phases. Dashed lines outline the positions of phase boundaries. (**E**) ADF-STEM images (top row) and EDS mapping (bottom row) of representative triphase NPs for all phase combinations. The compositions of the four triphase NPs are $Au_{0.30}Ag_{0.19}Cu_{0.29}Co_{0.22}$, $Au_{0.12}Ag_{0.30}Cu_{0.28}Pd_{0.20}Sn_{0.10}$, $Au_{0.06}Ag_{0.10}Co_{0.24}Pd_{0.39}Sn_{0.21}$, and $Au_{0.13}Cu_{0.27}Co_{0.30}Pd_{0.15}Sn_{0.15}$. (**F**) ADF-STEM image (top row) and EDS mapping (bottom row) of a representative tetraphase NP composed of AuAg, AuCu, Co, and PdSn phases ($Au_{0.18}Ag_{0.16}Cu_{0.20}Co_{0.23}Pd_{0.13}Sn_{0.10}$). Overlay of selected element maps (middle row) shows the relative configuration of the four phases in the NP. Dashed lines highlight the positions of the five phase boundaries. Scale bars, 15 nm.

Interface engineering in tetraphase NPs

Observation 4: Interfaces not observed in triphase NPs do not exist in higher-order multiple (four or more)–phase NPs.

Predicting the architecture of tetraphase heterostructured NPs with four distinct metal phases by using DFT simulations is challenging because such particles will have four distinct types of surfaces, defined by the different phases that constitute them, and up to six interfaces. Such a simulation must compare the surface energies of four phases and the interfacial energies of six interfaces and account for defects present near interfaces. Because a tetraphase NP can always be broken down into four constituent triphase NPs, experimentally the architecture of the four triphase NPs (either two or three interface) will be predictive of the thermodynamic architecture of the tetraphase NP. With PdSn as the basic building block, we synthesized and characterized all 31 types of multiphase NPs consisting of Au, Ag, Cu, Co, Ni, and PdSn (figs. S27 to S32). In addition to Au and Co, Ag, Cu, and Ni phase-segregated with PdSn, forming Ag-PdSn, $Cu_{0.92}Pd_{0.08}$-$Cu_{0.2}(PdSn)_{0.8}$, and $Ni_{0.6}Sn_{0.4}$-$Ni_{0.08}(PdSn)_{0.92}$ heterodimers, respectively. The phase segregation in these particles can be explained by the thermodynamically stable phases evaluated with the GCLP method (table S2). To confirm that triphase NP architectures could be used to predict tetraphase NP architectures, we synthesized tetraphase NPs by selecting triphase NP combinations that would yield increasingly complex architectures (Figs. 4 and 5).

The first NP combination we explored included two triphase NPs with two interfaces and two triphase NPs with three interfaces (Fig. 4A). A system consisting of Ag, Cu, Co, and PdSn matches this scenario, where Ag-Cu-Co and PdSn-Cu-Co are two-interface heterotrimers and Ag-Cu-PdSn and Ag-Co-PdSn are three-interface heterotrimers, as observed in the ADF-STEM images and EDS elemental mapping of every triphase NP (Fig. 4B and fig. S33). The architectures of the four triphase NPs suggest that the interfaces between Ag and Co and between PdSn and Co were energetically unfavorable compared with the other four interfaces and four surfaces, which should prevent the formation of such interfaces when the tetraphase NP reaches a thermodynamic configuration. To test this prediction, we synthesized Ag-Cu-Co-PdSn NPs and investigated their structures by ADF-STEM and EDS. The majority (architectural yield, ~70%; sample size, 30) of Ag-Cu-Co-PdSn NPs had architectures as predicted (Fig. 4C and fig. S34). The Cu domain in the center of the NP separated the Co domain from the Ag and PdSn domains, thus avoiding the formation of Ag-Co and PdSn-Co interfaces. However, the three interfaces among Cu, Ag, and PdSn domains connected with one another, forming a triphase junction. Tetraphase NPs with this combination of triphase architectures adopt an architecture with four interfaces and one triphase junction.

The second NP combination consists of one triphase NP with two interfaces whereas the

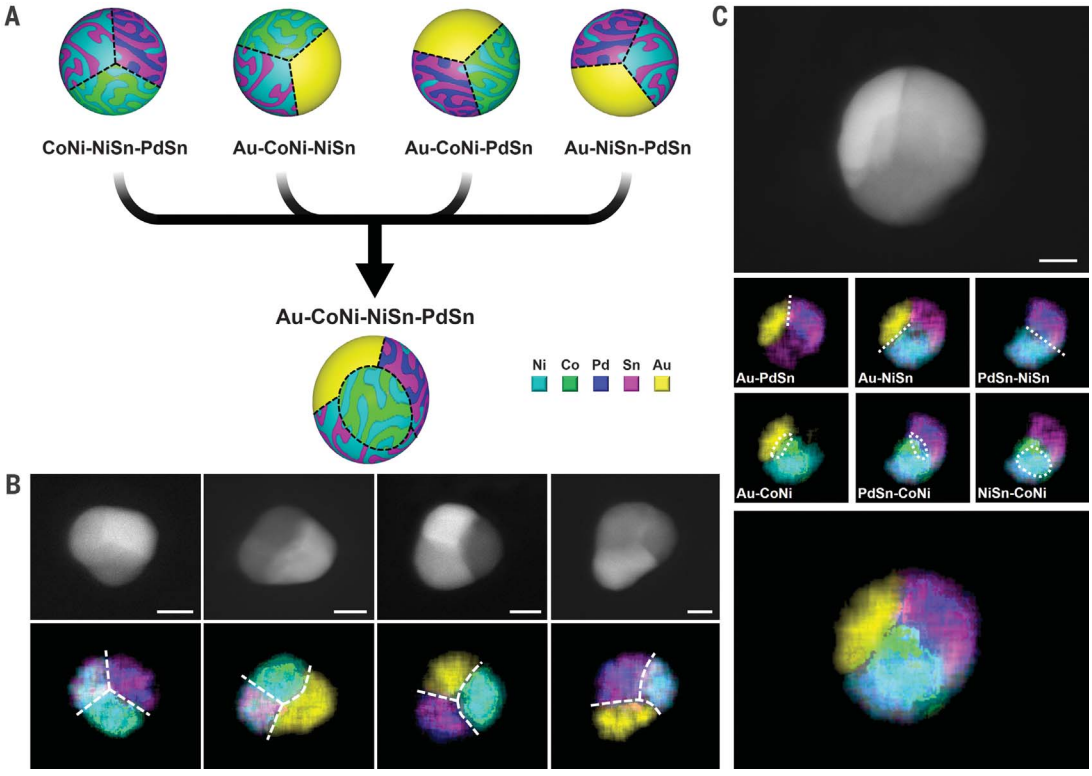

Fig. 5. Tetraphase heterostructured NPs with six interfaces. (**A**) Schematic illustration depicting the architectures of tri- and tetraphase NPs composed of Au, CoNi, NiSn, and PdSn phases. Dashed lines outline the positions of the phase boundaries. (**B**) ADF-STEM images (top row) and EDS mapping (bottom row) of representative triphase NPs for all phase combinations. The compositions of the four triphase NPs are $Co_{0.13}Ni_{0.35}Pd_{0.26}Sn_{0.26}$, $Au_{0.37}Co_{0.18}Ni_{0.36}Sn_{0.09}$, $Au_{0.29}Co_{0.17}Ni_{0.19}Pd_{0.20}Sn_{0.15}$, and $Au_{0.25}Ni_{0.24}Pd_{0.20}Sn_{0.31}$. (**C**) ADF-STEM image (top row) and EDS mapping (bottom row) of a representative tetraphase NP composed of Au, CoNi, NiSn, and PdSn phases ($Au_{0.20}Co_{0.11}Ni_{0.30}Pd_{0.21}Sn_{0.18}$). Overlay of selected elemental maps (two middle rows) shows the relative positions of any two of the four phases. Dashed lines and circles outline the positions of the six phase boundaries in the NP. Scale bars, 15 nm.

other three triphase NPs have three interfaces (Fig. 4D). The triphase combinations of AuAg, AuCu, Co, and PdSn satisfy this category, where AuAg-AuCu-Co formed a striped two-interface heterotrimer and AuAg-AuCu-PdSn, AuAg-PdSn-Co, and AuCu-PdSn-Co formed three-interface heterotrimers. The architecture of every triphase NP was verified by ADF-STEM characterization and EDS elemental mapping (Fig. 4E and fig. S35). The only striped NP (AuAg-AgCu-Co) in this combination type suggests that only one interface was energetically unfavored when forming a tetraphase NP. AuAg-AuCu-PdSn-Co NPs were synthesized to confirm the prediction. As shown in Fig. 4F and figs. S36 and S37, AuCu and PdSn domains were in the center of the particle, with AuAg and Co domains capped on each end (architectural yield, ~70%; sample size, 30). One triphase junction formed among the AuAg, AuCu, and PdSn phases. The other triphase junction formed among the AuCu, PdSn, and Co phases. Tetraphase NPs with this combination of triphase NP types have an architecture with five interfaces and two triphase junctions.

As a final demonstration of interface engineering in polyelemental NPs, we used a system where all four triphase NPs shared the same configurational feature: a three-interface architecture (pie-shaped structures in Fig. 5A). The architecture of the four triphase NPs suggests that all six interfaces and four surfaces were energetically compatible with one another. The structures of triphase NPs containing Au, CoNi, NiSn, and PdSn phases provide a guide for predicting the thermodynamic structure of the single tetraphase structure, which could have as many as six interfaces (Fig. 5B and fig. S38). The incorporation of these four phases into one NP leads to an unprecedented nanostructure with four constituent domains interfaced with one another (architectural yield, ~65%; sample size, 30) (Fig. 5C and figs. S39 to S42). The overlay of EDS element maps revealed the identity and distribution of the four phases and their spatial relationship in one typical NP. The Au, PdSn, and NiSn domains interconnected with one another, whereas the CoNi domain sat on top of the other three domains, forming six phase boundaries in one particle (Fig. 5C and fig. S39). Tetraphase NPs with this combination of triphase particle types have an architecture with six interfaces, four triphase junctions, and one tetraphase junction point that is embedded in a single NP. This study shows that NP phase hierarchy can be used for engineering the number and types of phase boundaries in higher-order structures.

Discussion

We have presented a set of four rules for engineering the number and types of interfaces in multiphase polyelemental NPs by using PdSn-based multiphase NPs as a proof-of-concept system. For interface engineering, the balancing of surface and interfacial energies is critical in determining the thermodynamically preferred structures for multiphase NPs, as demonstrated by the notable tetraphase polyelemental NPs described herein, with four, five, and six phase boundaries. Looking forward, these guidelines will be particularly useful in elucidating the complex architectures of NPs containing more than four phases, where the NPs may have 10 or more different interfaces. Interface engineering in polyelemental nanomaterials will be essential for optimizing their use in catalysis, plasmonics, nanoelectronics, and energy harvesting, and challenges moving forward are to establish high-throughput ways for characterizing their properties, as a function of composition, size, phase, and architecture, and to develop methods for their scalable syntheses (*1*, *2*, *18*, *20*, *21*).

REFERENCES AND NOTES

1. M. R. Buck, J. F. Bondi, R. E. Schaak, *Nat. Chem.* **4**, 37–44 (2012).
2. L. Weng, H. Zhang, A. O. Govorov, M. Ouyang, *Nat. Commun.* **5**, 4792 (2014).
3. Z. C. Zhang, B. Xu, X. Wang, *Chem. Soc. Rev.* **43**, 7870–7886 (2014).
4. D. Rodríguez-Fernández, J. Langer, M. Henriksen-Lacey, L. M. Liz-Marzán, *Chem. Mater.* **27**, 2540–2545 (2015).
5. Q. Fu, T. Wagner, *Surf. Sci. Rep.* **62**, 431–498 (2007).
6. C. T. Campbell, *Nat. Chem.* **4**, 597–598 (2012).
7. X. Ye *et al*., *J. Am. Chem. Soc.* **136**, 5106–5115 (2014).
8. M. Lin, G. H. Kim, J. H. Kim, J. W. Oh, J. M. Nam, *J. Am. Chem. Soc.* **139**, 10180–10183 (2017).
9. Y. Sun, J. J. Foley 4th, S. Peng, Z. Li, S. K. Gray, *Nano Lett.* **13**, 3958–3964 (2013).
10. C. George *et al*., *Nano Lett.* **13**, 752–757 (2013).
11. L. Li *et al*., *Angew. Chem. Int. Ed. Engl.* **52**, 11049–11053 (2013).
12. S. Najafishirtari *et al*., *J. Catal.* **338**, 115–123 (2016).
13. H. Wang *et al*., *Science* **354**, 1031–1036 (2016).
14. I. X. Green, W. Tang, M. Neurock, J. T. Yates Jr., *Science* **333**, 736–739 (2011).
15. C. W. Li, J. Ciston, M. W. Kanan, *Nature* **508**, 504–507 (2014).
16. C. Xie *et al*., *Nano Lett.* **17**, 3798–3802 (2017).
17. P. V. Kamat, *J. Phys. Chem. Lett.* **3**, 663–672 (2012).
18. X. Liu *et al*., *Nano Lett.* **12**, 5733–5739 (2012).
19. P.-C. Chen *et al*., *Science* **352**, 1565–1569 (2016).
20. Y. Yao *et al*., *Science* **359**, 1489–1494 (2018).
21. J. L. Fenton, B. C. Steimle, R. E. Schaak, *Science* **360**, 513–517 (2018).
22. H. T. Zhang, J. Ding, G. M. Chow, Z. L. Dong, *Langmuir* **24**, 13197–13202 (2008).
23. X. F. Li, R. E. Schaak, *Chem. Mater.* **29**, 4153–4160 (2017).
24. J. M. Hodges, R. E. Schaak, *Acc. Chem. Res.* **50**, 1433–1440 (2017).
25. R. Costi, A. E. Saunders, U. Banin, *Angew. Chem. Int. Ed. Engl.* **49**, 4878–4897 (2010).
26. Y. Min, J. Kwak, A. Soon, U. Jeong, *Acc. Chem. Res.* **47**, 2887–2893 (2014).
27. M. Casavola *et al*., *Nano Lett.* **9**, 366–376 (2009).
28. P.-C. Chen *et al*., *J. Am. Chem. Soc.* **137**, 9167–9173 (2015).
29. H. Wu *et al*., *J. Am. Chem. Soc.* **133**, 14327–14337 (2011).
30. S. Peng, C. Lei, Y. Ren, R. E. Cook, Y. Sun, *Angew. Chem. Int. Ed. Engl.* **50**, 3158–3163 (2011).
31. P. Villars, H. Okamoto, K. Cenzual, Eds., *ASM Alloy Phase Diagrams Database* (ASM International, 2006).
32. J. E. Saal, S. Kirklin, M. Aykol, B. Meredig, C. Wolverton, *JOM* **65**, 1501–1509 (2013).
33. S. Kirklin *et al*., *NPJ Comput. Mater.* **1**, 15010 (2015).
34. S. Kirklin, B. Meredig, C. Wolverton, *Adv. Energy Mater.* **3**, 252–262 (2013).
35. P.-C. Chen *et al*., *J. Am. Chem. Soc.* **139**, 9876–9884 (2017).

ACKNOWLEDGEMENTS

Funding: This material is based upon work supported by the Sherman Fairchild Foundation; the Air Force Office of Scientific Research under award FA9550-17-1-0348; and the Vannevar Bush Faculty Fellowship program, sponsored by the Basic Research Office of the Assistant Secretary of Defense for Research and Engineering and funded by the Office of Naval Research through grant N00014-15-1-0043. M.L. and C.W. acknowledge support from Toyota Research Institute through the Accelerated Materials Design and Discovery program. This work made use of resources in the National Energy Research Scientific Computing Center (NERSC) and Northwestern University's Quest high-performance computing system. This work made use of the EPIC facility of Northwestern University's NUANCE Center, which has received support from the Soft and Hybrid Nanotechnology Experimental (SHyNE) Resource (NSF ECCS-1542205), the MRSEC program (NSF DMR-1720139) at the Materials Research Center, the International Institute for Nanotechnology (IIN), the Keck Foundation, and the State of Illinois through the IIN. **Author contributions:** P.-C.C. and C.A.M. conceived the ideas and designed the experiments. P.-C.C. performed particle synthesis and conducted STEM analysis. M.L. and C.W. designed and performed the DFT calculations. P.-C.C. and J.S.D. conducted HRTEM characterization. P.-C.C., J.S.D., B.M., S.W., H.L., V.P.D., and C.A.M. analyzed electron microscopy characterization results. C.A.M. and P.-C.C. wrote the manuscript with editorial input from the other authors. C.A.M. supervised the project. **Competing interests:** A provisional patent application has been filed on this work. **Data and materials availability:** All data are available in the main text or the supplementary materials.

SUPPLEMENTARY MATERIALS

www.sciencemag.org/content/363/6430/959/suppl/DC1
Materials and Methods
Supplementary Text
Figs. S1 to S42
Tables S1 to S5
References (*36*–*41*)

14 September 2018; resubmitted 17 December 2018
Accepted 1 February 2019
10.1126/science.aav4302

Interface and heterostructure design in polyelemental nanoparticles

Peng-Cheng Chen, Mohan Liu, Jingshan S. Du, Brian Meckes, Shunzhi Wang, Haixin Lin, Vinayak P. Dravid, Chris Wolverton and Chad A. Mirkin

Science **363** (6430), 959-964.
DOI: 10.1126/science.aav4302

Phases of multielement nanoparticles

Thermodynamically stable metal nanoparticles composed of multiple elements could, in principle, exhibit several different phases that form multiple interfaces. Chen *et al.* explored the structure and composition of palladium-tin alloy nanoparticles formed with up to five other elements after high-temperature annealing. Triphase nanoparticles possessed two or three interface architectures, and tetraphase nanoparticles exhibited up to six interfaces. Theoretical and experimental studies revealed how the balance between surface and interfacial energies influences the observed phases and interface structure.

Science, this issue p. 959